Consideration on Singular-Point Generating Mechanisms by Analyzing the Effect of Phase-and-Polarization Optimization in PolInSAR

Yuta Otsuka, Tomoharu Shimada, Ryo Natsuaki, *Member, IEEE*, and Akira Hirose, *Fellow, IEEE*

***Abstract*—We elucidate the generation mechanisms of singular points (SPs) by investigating the relationship between the phase distortion and the polarization-state changes in polarimetric interferometric synthetic aperture radar (PolInSAR). We find that there is a high correlation between the parameters in the Pauli coherency matrix and those in the scattering mechanism vector optimized by the maximization of interferometric coherence. It means that there is a correlation between the parameters of polarization and those of the phase compensation. In other words, the main changes in phase and those in polarization are caused by an identical phenomenon, that is, scattering itself. Therefore, we can use the parameters of polarization to reduce SPs. We also find that other origins that cause the changes in phase are the interference of waves from multiple scattering sources and thermal noise. Lastly, we investigate how the optimization compensates polarization changes by introducing the scattering sphere representation. We find that the optimization reduces randomness in the polarimetric features, and enhances the features specific to deterministic scattering such as surface and double-bounce scattering. It means that probabilistic/random scattering is the main origin of SP generation.**

***Index Terms*—Interferometric synthetic aperture radar (InSAR), polarimetric interferometric synthetic aperture radar (PolInSAR), singular points (SPs).**

I. Introduction

SYNTHETIC aperture radar (SAR) plays a significant role in the remote-sensing earth observation. SAR observations have been conducted globally targetting various areas such as polar regions, tropical areas, and the ocean [1], [2].

Interferometric synthetic aperture radar (InSAR) is one of the SAR techniques. InSAR observes an identical earth surface point from two satellite positions and generates an interferogram by calculating the phase differences of two complex-valued data. Because the phase differences between neighboring pixels correspond to the height changes, the phase value of each pixel is the remainder of a land height divided by geometric parameters. It is wrapped with a period of 2π. A digital elevation model (DEM) can be generated by unwrapping this folded phase image. Since the land height forms a vector field whose curl is zero, it is a conservative field. Therefore, the unwrapping process should be conducted easily by integrating the differences of neighboring pixels.

However, rotational points, that is, singular points (SPs) make it difficult to generate DEMs. When a SP exists, the estimated height is dependent on the integration path. We have to minimize the total length of branch-cuts [3], which the integration path should not cross, since the branch-cuts result in artificial cliffs. This minimization requires a high calculation cost. To solve this problem, a lot of methods have been proposed such as unwrapping methods [4]–[10], filtering methods [11]–[17], local registration methods [18]–[21] and methods using polarimetric interferometric SAR (PolInSAR) [22]–[26].

Previously, we proposed an optimization method based on the linear combination of respective polarization data [27], [28], which reduces the number of SPs drastically by considering the pixel-by-pixel variety of the scattering mechanisms. The method was named pixel-by-pixel optimization considering baseline difference (PPO-BD).

In this article, we elucidate the singular-point generating mechanisms by analyzing the results of PPO-BD. The analysis will also be useful for creating a more effective filter to reduce SPs. Although the singular-point generating mechanisms have been studied in many ways [29]–[31], this is the first article to investigate the singular-point generating mechanisms by focusing on the relationship between polarization and phase. The results of the analysis show that scattering itself causes the changes in the phase and eventually SPs. This fact is clarified by the coincidence of the parameters in the Pauli coherency matrix and those in the scattering mechanism vectors optimized by the maximization of the coherence in the interferogram. We also investigate other origins that cause the changes in phase. We find that they are the interference of waves from multiple scattering sources and the thermal noise. Lastly, we investigate how PPO-BD compensates the polarimetric changes caused by scattering. We find that PPO-BD reduces randomness and enhances the polarimetric features specific to deterministic scattering such as surface and double-bounce scattering. It means

Manuscript received June 14, 2019; revised December 23, 2019, February 18, 2020, and March 22, 2020; accepted March 23, 2020. Date of publication April 13, 2020; date of current version May 11, 2020. This work was supported in part by JSPS KAKENHI under Grant 5H02756 and Grant 18H04105, in part by KDDI Foundation, and in part by Cooperative Research Project Program of the Research Institute of Electrical Communication, Tohoku University. This paper was presented in part at the Photonics and Electromagnetics Research Symposium, Toyama International Conference Center and ANA Crowne Plaza Toyama, Toyama, Japan, August 2018. *(Corresponding author: Yuta Otsuka.)*

The authors are with the Department of Electrical Engineering and Information Systems, The University of Tokyo, Tokyo 113-8656, Japan (e-mail: otsuka_yuta@eis.t.u-tokyo.ac.jp; t_shimada@eis.t.u-tokyo.ac.jp; natsuaki@eis.t.u-tokyo.ac.jp; ahirose@ee.t.u-tokyo.ac.jp).

Digital Object Identifier 10.1109/JSTARS.2020.2983801

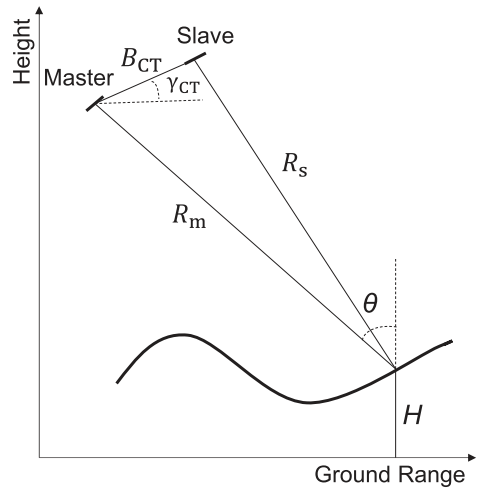

Fig. 1. Illustration showing InSAR observation of the land surface (curve) from two satellite points (Master and Slave) to obtain master and slave images for generation of an interferogram.

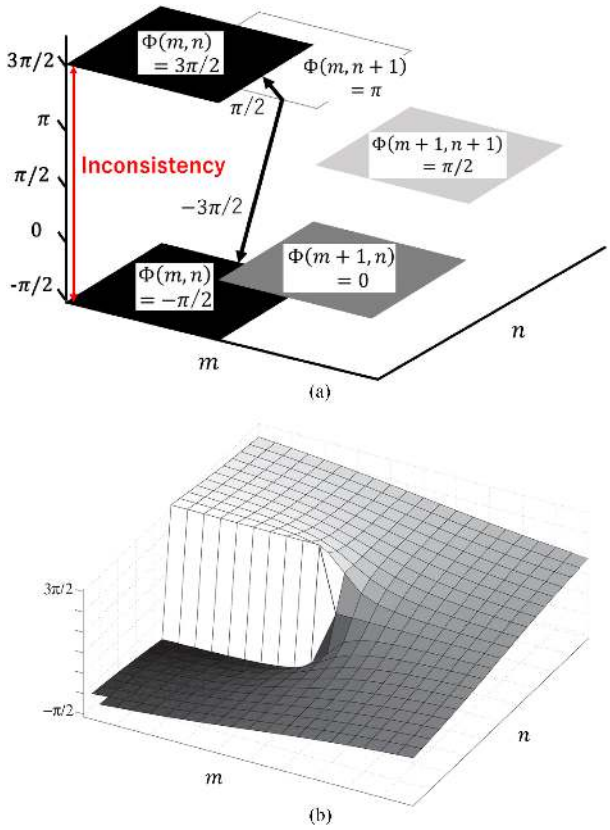

Fig. 2. Conceptual illustration showing (a) four pixels constructing a SP ($-\pi/2$ pixel is identical to $3\pi/2$ pixel) and (b) its DEM.

that probabilistic/random scattering is the main origin of SP generation.

This rest of the article is organized as follows. Section II reviews the interferometric SAR and singular points. Section III describes the processing details of conventional methods of PolInSAR and PPO-BD. Section IV analyzes singular-point generation mechanisms. Section V interprets and discusses the results further. Section VI is the conclusion of this article.

II. Interferometric SAR and Singular Points

Fig. 1 shows the overview of the InSAR observation. First, SAR observes an identical earth surface area from two satellite positions to get two complex-amplitude images, namely, a master image and a slave image. The phase of an interferogram represents the phase difference of the master and slave images, corresponding to the distance from the antenna to the land surface. Then the land height difference ΔH is calculated by the phase difference $\Delta\Phi$ by using the distance from one of the antennas to the land surface $R_{\rm m}$, the distance between the antennas (baseline) $B_{\rm CT}$, baseline elevation angle $\gamma_{\rm CT}$ and the wavelength λ as

$$\Delta H = \frac{\lambda R_{\rm m} \sin\theta}{4\pi B_{\rm CT}\cos(\theta - \gamma_{\rm CT})}\Delta\Phi \tag{1}$$

where θ is the off-nadir angle. We can calculate the land height by integrating the phase differences of neighboring pixels in the interferogram.

As seen above, an interferogram in InSAR is generated by calculating a product of master and conjugated slave images. The phase is wrapped into $(-\pi, \pi]$. Then we need to unwrap it. Since the land height forms a conservative field, the integral value for a closed-loop should be zero. However, it is not zero around a SP. Then we cannot determine the land height uniquely when there is a SP. Fig. 2 shows a conceptual illustration showing four pixels constructing a SP and its DEM. In Fig. 2(a), the phase values are $\Phi(m,n) = -\pi/2$, $\Phi(m+1,n) = 0$, $\Phi(m+1,n+1) = \pi/2$, $\Phi(m,n+1) = \pi$. Assume that we integrate the phase differences of the four pixels in this order. Since the phase differences from $\Phi(m,n)$ to $\Phi(m+1,n)$, from $\Phi(m+1,n)$ to $\Phi(m+1,n+1)$, and from $\Phi(m+1,n+1)$ to $\Phi(m,n+1)$ are $\pi/2$, we can consider this integral path as an upward slope. Then the integral path from $\Phi(m,n+1)$ to $\Phi(m,n)$ shows a downward slope with the phase change of $-3\pi/2$ apparently. But, by considering the periodicity of phase, we take the principal value for this phase change as $\pi/2$. The integral value of this closed route is 2π showing a rotation. This is a SP. Thus, we cannot determine the land height. If we make a DEM forcibly, the result will lead to an artificial cliff like that in Fig. 2(b). We therefore, need to reduce artificial cliff-making SPs to generate accurate DEMs. However, the generation mechanisms of SPs are not fully clear [29], [30].

III. Polarization Diversity

Researchers studied the combination of interferometric information in multiple polarimetric channels in PolInSAR to reduce artificial SPs. PolInSAR observes scattering coefficients to construct a scattering matrix as

$$\mathbf{S} = \begin{bmatrix} S_{\rm HH} & S_{\rm HV} \\ S_{\rm VH} & S_{\rm VV} \end{bmatrix} \tag{2}$$

where S_{ij} (i, j = H or V) is the coefficient for j transmitted and i received polarization electromagnetic waves in the HV-polarimetric basis. In the case of monostatic radar, we can

assume that S_{HV} is equal to S_{VH}. The scattering matrix is equivalently replaced by the Pauli scattering vector

$$\boldsymbol{k} = \frac{1}{\sqrt{2}} \begin{bmatrix} S_{\mathrm{HH}} + S_{\mathrm{VV}} \\ S_{\mathrm{HH}} - S_{\mathrm{VV}} \\ 2S_{\mathrm{HV}} \end{bmatrix}. \tag{3}$$

The coherency matrix is calculated by the scattering vector as eq. (4) shown at the bottom of this page, where n is the pixel number included in a local window for coherency calculation. The Pauli coherency matrix can be diagonalized by using a unitary matrix as

$$[T] = \frac{1}{n} \sum^{n} \boldsymbol{k}\boldsymbol{k}^{*} = [U_3] \begin{bmatrix} \lambda_1 & 0 & 0 \\ 0 & \lambda_2 & 0 \\ 0 & 0 & \lambda_3 \end{bmatrix} [U_3]^{*}$$

$$= \sum_{i=1}^{3} \lambda_i \boldsymbol{e}_i \boldsymbol{e}_i^{*} \tag{5}$$

where $\lambda_i (i = 1, 2, 3)$ denote eigenvalues and $[U_3]$ is expressed as [32] eq. (6) shown at the bottom of this page.

The scattering-mechanism probabilities P_i corresponding to the eigenvalues are defined as [32]

$$P_i = \frac{\lambda_i}{\lambda_1 + \lambda_2 + \lambda_3}. \tag{7}$$

The entropy H and angle $\overline{\alpha_{\mathrm{cm}}}$, which are often used for land classification, are defined as [32]

$$H = -P_1 \log_3 P_1 - P_2 \log_3 P_2 - P_3 \log_3 P_3 \tag{8}$$

$$\overline{\alpha_{\mathrm{cm}}} = P_1 \alpha_{\mathrm{cm}_1} + P_2 \alpha_{\mathrm{cm}_2} + P_3 \alpha_{\mathrm{cm}_3}. \tag{9}$$

The entropy H shows the randomness of scattering while the angle $\overline{\alpha_{\mathrm{cm}}}$ represents the dominant scattering mechanism, ranging from 0° for surface scattering, 45° for linear dipole scattering and to 90° for dihedral scatterer. One of the methods in PolInSAR was proposed by Cloude and Papathanassiou [32]. This method makes the most of the polarimetric information by taking a linear combination of polarization. The flow of the processing is explained as follows. A Hermitian positive semidefinite matrix is defined by using the master Pauli vector $\boldsymbol{k}_{\mathrm{m}}$ and the slave Pauli vector $\boldsymbol{k}_{\mathrm{s}}$ as

$$[T_6] = \left\langle \begin{bmatrix} \boldsymbol{k}_{\mathrm{m}} \\ \boldsymbol{k}_{\mathrm{s}} \end{bmatrix} \begin{bmatrix} \boldsymbol{k}_{\mathrm{m}}^{*} & \boldsymbol{k}_{\mathrm{s}}^{*} \end{bmatrix} \right\rangle = \begin{bmatrix} [T_{\mathrm{mm}}] & [\Omega_{\mathrm{ms}}] \\ [\Omega_{\mathrm{ms}}]^{*} & [T_{\mathrm{ss}}] \end{bmatrix} \tag{10}$$

where $[T_{\mathrm{mm}}]$, $[T_{\mathrm{ss}}]$ and $[\Omega_{\mathrm{ms}}]$ are given by

$$[T_{\mathrm{mm}}] = \langle \boldsymbol{k}_{\mathrm{m}} \boldsymbol{k}_{\mathrm{m}}^{*} \rangle,\ [T_{\mathrm{ss}}] = \langle \boldsymbol{k}_{\mathrm{s}} \boldsymbol{k}_{\mathrm{s}}^{*} \rangle,\ [\Omega_{\mathrm{ms}}] = \langle \boldsymbol{k}_{\mathrm{m}} \boldsymbol{k}_{\mathrm{s}}^{*} \rangle. \tag{11}$$

New complex scattering coefficients can be generated by calculating the product of a 3×1 arbitrary complex unit vectors, $\boldsymbol{w}_{\mathrm{m}}$ and $\boldsymbol{w}_{\mathrm{s}}$, and Pauli vectors, $\boldsymbol{k}_{\mathrm{m}}$ and $\boldsymbol{k}_{\mathrm{s}}$, as

$$\mu_{\mathrm{m}} = \boldsymbol{w}_{\mathrm{m}}^{*} \boldsymbol{k}_{\mathrm{m}},\ \ \mu_{\mathrm{s}} = \boldsymbol{w}_{\mathrm{s}}^{*} \boldsymbol{k}_{\mathrm{s}}. \tag{12}$$

The vectors $\boldsymbol{w}_{\mathrm{m}}$ and $\boldsymbol{w}_{\mathrm{s}}$ are called the scattering mechanism vectors. We calculate the interferometric phase of the interferogram by using these new coefficients as

$$\Phi_{\mathrm{Cloude}} = \arg\{\mu_{\mathrm{m}} \mu_{\mathrm{s}}^{*}\} = \arg\{\boldsymbol{w}_{\mathrm{m}}^{*} [\Omega_{\mathrm{ms}}] \boldsymbol{w}_{\mathrm{s}}\}. \tag{13}$$

The interferometric coherence is given by

$$\gamma_{\mathrm{Cloude}} = \frac{|\langle \mu_{\mathrm{m}} \mu_{\mathrm{s}}^{*} \rangle|}{\sqrt{\langle \mu_{\mathrm{m}} \mu_{\mathrm{m}}^{*} \rangle \langle \mu_{\mathrm{s}} \mu_{\mathrm{s}}^{*} \rangle}}$$

$$= \frac{|\langle \boldsymbol{w}_{\mathrm{m}}^{*} [\Omega_{\mathrm{ms}}] \boldsymbol{w}_{\mathrm{s}} \rangle|}{\sqrt{\langle \boldsymbol{w}_{\mathrm{m}}^{*} [T_{\mathrm{mm}}] \boldsymbol{w}_{\mathrm{m}} \rangle \langle \boldsymbol{w}_{\mathrm{s}}^{*} [T_{\mathrm{ss}}] \boldsymbol{w}_{\mathrm{s}} \rangle}}. \tag{14}$$

We optimize $\boldsymbol{w}_{\mathrm{m}}$ and $\boldsymbol{w}_{\mathrm{s}}$ as the linear combination of polarization states that yields the highest coherence. It is given by solving a 3×3 complex eigenvalue problem expressed as

$$[T_{\mathrm{ss}}]^{-1} [\Omega_{\mathrm{ms}}]^{*} [T_{\mathrm{mm}}]^{-1} [\Omega_{\mathrm{ms}}] \boldsymbol{w}_{\mathrm{s}} = \nu \boldsymbol{w}_{\mathrm{s}} \tag{15}$$

$$[T_{\mathrm{mm}}]^{-1} [\Omega_{\mathrm{ms}}] [T_{\mathrm{ss}}]^{-1} [\Omega_{\mathrm{ms}}]^{*} \boldsymbol{w}_{\mathrm{m}} = \nu \boldsymbol{w}_{\mathrm{m}}. \tag{16}$$

Here, Tabb *et al.* further proposed to assume $[T_{\mathrm{mm}}] \approx [T_{\mathrm{ss}}]$[33]. They reported that the interferograms generated with this method have fewer SPs than those with Cloude's method, resulting in a more accurate DEM.

The conventional methods assumed multi-look interferograms to generate DEMs. Since the resolution of SAR has been being improved significantly, now it is desirable that we can make DEMs by using single-look interferograms, if possible. In Cloude's method as well as Tabb's method, the scattering mechanism vectors $\boldsymbol{w}$'s are homogeneous in the local window though the value should actually vary pixel by pixel in single-look interferograms. Then, we proposed a method to optimize $\boldsymbol{w}$'s pixel by pixel, that is, PPO-BD (Pixel-by-Pixel Optimization considering Baseline Difference) [27]. The processing flow of this method is shown as follows.

1) Calculate the scattering mechanism vectors $\boldsymbol{w}_{\mathrm{m}}(x, y)$ and $\boldsymbol{w}_{\mathrm{s}}(x, y)$ at position (x, y) by Tabb's method for the whole target area to be used below as the initial vector $(\boldsymbol{w}_{\mathrm{m}}(x, y) = \boldsymbol{w}_{\mathrm{s}}(x, y) = \boldsymbol{w}(x, y))$.
2) Update only the scattering mechanism vectors of (X, Y), the center pixel in a 3×3 window, $\boldsymbol{w}_{\mathrm{m}}(X, Y)$ and $\boldsymbol{w}_{\mathrm{s}}(X, Y)$ respectively by maximizing the interferometric

$$[T] = \frac{1}{n} \sum^{n} \boldsymbol{k}\boldsymbol{k}^{*} = \frac{1}{2} \begin{bmatrix} \langle |S_{\mathrm{HH}} + S_{\mathrm{VV}}|^2 \rangle & \langle (S_{\mathrm{HH}} + S_{\mathrm{VV}}) (S_{\mathrm{HH}} - S_{\mathrm{VV}})^{*} \rangle & \langle 2S_{\mathrm{HV}}^{*} (S_{\mathrm{HH}} + S_{\mathrm{VV}}) \rangle \\ \langle (S_{\mathrm{HH}} - S_{\mathrm{VV}}) (S_{\mathrm{HH}} + S_{\mathrm{VV}})^{*} \rangle & \langle |S_{\mathrm{HH}} - S_{\mathrm{VV}}|^2 \rangle & \langle 2S_{\mathrm{HV}}^{*} (S_{\mathrm{HH}} - S_{\mathrm{VV}}) \rangle \\ \langle 2S_{\mathrm{HV}} (S_{\mathrm{HH}} + S_{\mathrm{VV}})^{*} \rangle & \langle 2S_{\mathrm{HV}} (S_{\mathrm{HH}} - S_{\mathrm{VV}})^{*} & 4|S_{\mathrm{HV}}|^2 \rangle \end{bmatrix} \tag{4}$$

$$[U_3] = [\boldsymbol{e}_1 \boldsymbol{e}_2 \boldsymbol{e}_3] = \begin{bmatrix} \cos \alpha_{\mathrm{cm}_1} e^{j\phi_{\mathrm{cm}_1}} & \cos \alpha_{\mathrm{cm}_2} e^{j\phi_{\mathrm{cm}_2}} & \cos \alpha_{\mathrm{cm}_3} e^{j\phi_{\mathrm{cm}_3}} \\ \sin \alpha_{\mathrm{cm}_1} \cos \beta_{\mathrm{cm}_1} e^{j\delta_{\mathrm{cm}_1}} & \sin \alpha_{\mathrm{cm}_2} \cos \beta_{\mathrm{cm}_2} e^{j\delta_{\mathrm{cm}_2}} & \sin \alpha_{\mathrm{cm}_3} \cos \beta_{\mathrm{cm}_3} e^{j\delta_{\mathrm{cm}_3}} \\ \sin \alpha_{\mathrm{cm}_1} \sin \beta_{\mathrm{cm}_1} e^{j\gamma_{\mathrm{cm}_1}} & \sin \alpha_{\mathrm{cm}_2} \sin \beta_{\mathrm{cm}_2} e^{j\gamma_{\mathrm{cm}_2}} & \sin \alpha_{\mathrm{cm}_3} \sin \beta_{\mathrm{cm}_3} e^{j\gamma_{\mathrm{cm}_3}} \end{bmatrix} \tag{6}$$

coherence $\gamma_{\text{PPO-BD}}(X, Y)$ as eq. (17) shown at the bottom of this page. Sweep the window to update $\boldsymbol{w}$ of all the pixels.

The interferograms generated with the PPO-BD method have much fewer SPs than the conventional methods, resulting in much more accurate DEMs [27]. In some cases, interferograms generated with PPO-BD have no SPs. That is, the optimization of the linear combination of polarization components with a criterion of high coherence reduces SPs drastically. These results suggest that polarization is involved in the generation mechanisms of SPs. In the next section, we investigate the relationship between the parameters in $\boldsymbol{w}_{\text{opt}_\text{m}}$ with those in the coherency matrix so that we will elucidate the generation mechanisms in Section V.

IV. Analysis of Singular-Point Generation Mechanisms

We analyze the singular-point generation mechanisms by using ALOS-2 data collected on October 12, 2014, and October 26, 2014, over Mt. Fuji, Japan. We chose three sample areas of Forest, Grassland and Scree for the analysis. Fig. 3 shows the backscatter image and the sample areas. Fig. 4 shows the interferograms of the three areas generated with PPO-BD and their DEMs. The maximum and minimum heights for Forest, Grassland, and Scree are 1261 m and 420 m, 1240 m and 1056 m, 2634 m, and 1897 m, respectively.

The optimized scattering mechanism vector $\boldsymbol{w}_{\text{opt}_\text{m}}$ is given by five parameters, that is, $\alpha_{\text{opt}_\text{m}}, \beta_{\text{opt}_\text{m}}, \phi_{\text{opt}_\text{m}}, \delta_{\text{opt}_\text{m}}$ and $\gamma_{\text{opt}_\text{m}}$ as

$$\boldsymbol{w}_{\text{opt}_\text{m}} = \begin{bmatrix} \cos\alpha_{\text{opt}_\text{m}} e^{j\phi_{\text{opt}_\text{m}}} \\ \sin\alpha_{\text{opt}_\text{m}} \cos\beta_{\text{opt}_\text{m}} e^{j\delta_{\text{opt}_\text{m}}} \\ \sin\alpha_{\text{opt}_\text{m}} \sin\beta_{\text{opt}_\text{m}} e^{j\gamma_{\text{opt}_\text{m}}} \end{bmatrix}. \tag{18}$$

We compare these parameters in $\boldsymbol{w}_{\text{opt}_\text{m}}$ with those in the coherency matrix when $n = 1$ (single pixel).

First, we investigate angle α. Fig. 5(⋆-1) shows $\overline{\alpha_{\text{cm}_\text{m}}}$ in the Pauli coherency matrix while (⋆-2) $\alpha_{\text{opt}_\text{m}}$ of $\boldsymbol{w}_{\text{opt}_\text{m}}$ is obtained by the optimization in PPO-BD. We find that the values of $\alpha_{\text{opt}_\text{m}}$ are very close to those of $\overline{\alpha_{\text{cm}_\text{m}}}$ at respective pixels in all the areas. The differences of these parameters in the areas of Forest, Field and Scree are within 0.1 rad for 75.2, 74.8 and 76.4 pixels, respectively. Second, we investigate angle β. Fig. 6(⋆-1) shows $\overline{\beta_{\text{cm}_\text{m}}}$ in the Pauli coherency matrix while (⋆-2) $\beta_{\text{opt}_\text{m}}$ of $\boldsymbol{w}_{\text{opt}_\text{m}}$ in PPO-BD. The values of $\beta_{\text{opt}_\text{m}}$ are very close to those of $\overline{\beta_{\text{cm}_\text{m}}}$ at respective pixels again. The differences of these parameters in the areas of Forest, Field and Scree are within 0.1 rad for 70.9, 70.3 and 72.3 pixels, respectively. Among these pixels, the 91.5, 91.2 and 91.1 pixels also present differences less than 0.1 rad between $\overline{\alpha_{\text{cm}_\text{m}}}$ and $\alpha_{\text{opt}_\text{m}}$. Fig. 7(⋆-1) shows the scatter diagrams of $\overline{\alpha_{\text{cm}_\text{m}}}$ and $\alpha_{\text{opt}_\text{m}}$ while (⋆-2) the scatter diagrams of $\overline{\beta_{\text{cm}_\text{m}}}$ and $\beta_{\text{opt}_\text{m}}$. The correlation coefficients in Fig. 7(⋆-1) and (⋆-2) for the areas of Forest, Field and Scree are 0.81 and 0.77, 0.81 and 0.75, and 0.82, and 0.78, respectively. There are high correlations in these diagrams.

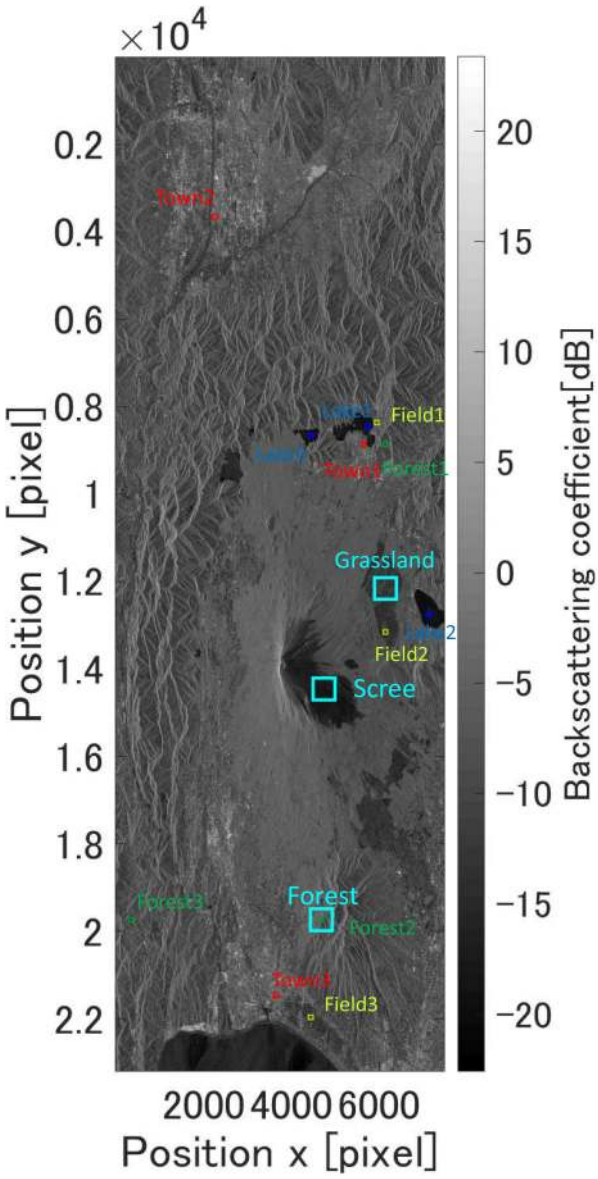

Fig. 3. Backscatter image with sample areas used in Section IV (Cyan) and Section V-D (Yellow green: Field, Red: Town, Dark green: Forest, Blue: Lake).

Finally, we investigate angle ϕ, δ and γ. Fig. 8(⋆-1) shows the scatter diagram of $\phi_{\text{opt}_\text{m}} - \overline{\phi_{\text{cm}_\text{m}}}$ and $\delta_{\text{opt}_\text{m}} - \overline{\delta_{\text{cm}_\text{m}}}$, Fig. 9(⋆-1) that of $\delta_{\text{opt}_\text{m}} - \overline{\delta_{\text{cm}_\text{m}}}$ and $\gamma_{\text{opt}_\text{m}} - \overline{\gamma_{\text{cm}_\text{m}}}$ and Fig. 10(⋆-1) that of $\delta_{\text{opt}_\text{m}} - \overline{\delta_{\text{cm}_\text{m}}}$ and $\gamma_{\text{opt}_\text{m}} - \overline{\gamma_{\text{cm}_\text{m}}}$. The correlation coefficients in Fig. 8(a-1), (b-1) and (c-1) are 0.67, 0.67 and 0.68, respectively. Those in Fig. 9(a-1), (b-1) and (c-1) are 0.56, 0.53, and 0.53, respectively. Those in Fig. 10(a-1), (b-1) and (c-1) are 0.59,

$$\gamma_{\text{PPO-BD}}(X, Y) = \frac{\left| \sum_{y=Y-1}^{Y+1} \sum_{x=X-1}^{X+1} \left(\boldsymbol{w}_\text{m}^*(x, y) \left[\Omega_\text{ms}(x, y) \right] \boldsymbol{w}_\text{s}(x, y) \right) \right|}{\sqrt{\sum_{y=Y-1}^{Y+1} \sum_{x=X-1}^{X+1} \left(\boldsymbol{w}_\text{m}^*(x, y) \left[T_\text{mm}(x, y) \right] \boldsymbol{w}_\text{m}(x, y) \right) \left(\boldsymbol{w}_\text{s}^*(x, y) \left[T_\text{ss}(x, y) \right] \boldsymbol{w}_\text{s}(x, y) \right)}} \tag{17}$$

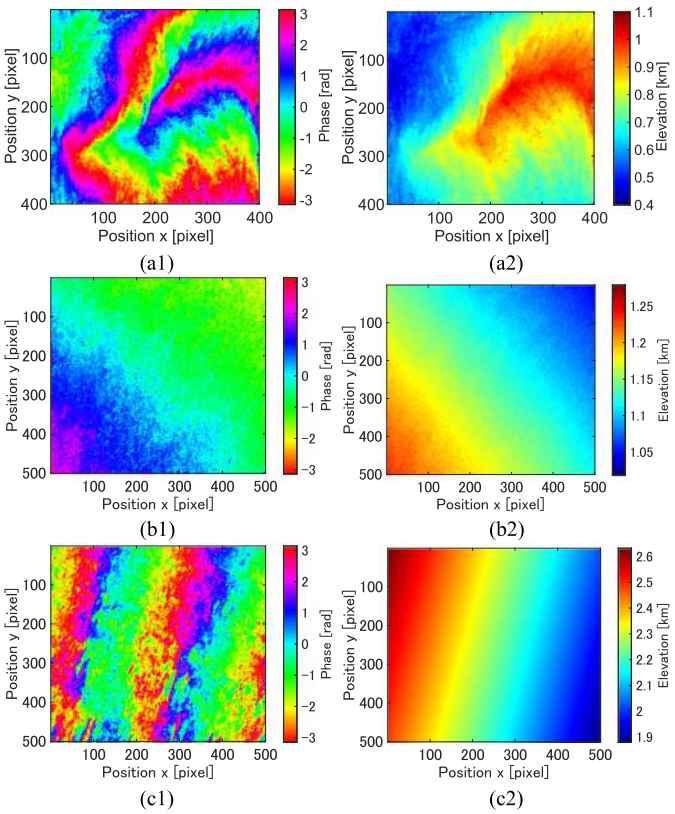

Fig. 4. (⋆-1) Interferograms generated with PPO-BD and (⋆-2) its DEM for the areas of (a-⋆) Forest, (b-⋆) Grassland, and (c-⋆) Scree.

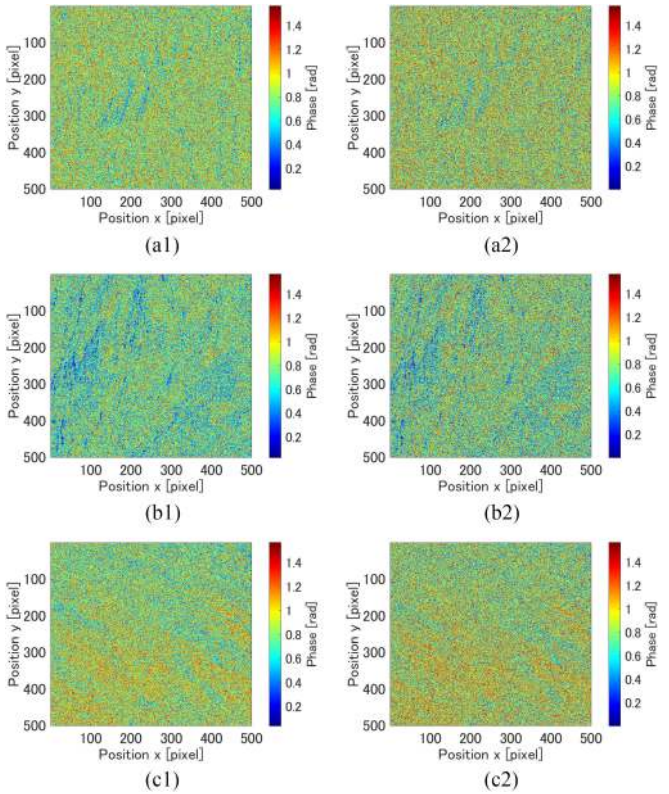

Fig. 5. (⋆-1) $\overline{\alpha_{\mathrm{cm_m}}}$ map in the Pauli coherency matrix and (⋆-2) $\alpha_{\mathrm{opt_m}}$ map of $\boldsymbol{w}_{\mathrm{opt_m}}$ in PPO-BD for the areas of (a-⋆) Forest, (b-⋆) Grassland, and (c-⋆) Scree.

0.55, and 0.54, respectively. There are high correlations in these diagrams.

Note that we argue these difference values since one of the three parameters is arbitrary. That is, since we cannot determine $\overline{\phi_{\mathrm{cm_m}}}$, $\overline{\delta_{\mathrm{cm_m}}}$ and $\overline{\gamma_{\mathrm{cm_m}}}$ uniquely, we show these diagrams with $\overline{\gamma_{\mathrm{cm_m}}}$ being 0 (or π), resulting in the vertical high-density lines at $\gamma_{\mathrm{opt_m}} - \overline{\gamma_{\mathrm{cm_m}}} = 0$ and π in (⋆-1) of Figs. 9 and 10.

These results mean that there are correlations between the set of $\overline{\phi_{\mathrm{cm_m}}}$, $\overline{\delta_{\mathrm{cm_m}}}$, $\overline{\gamma_{\mathrm{cm_m}}}$ and the other set of $\phi_{\mathrm{opt_m}}$, $\delta_{\mathrm{opt_m}}$, $\gamma_{\mathrm{opt_m}}$. Figs. 8(⋆-2), 9(⋆-2) and 10(⋆-2) show the scatter diagrams generated by replacing $\overline{\phi_{\mathrm{cm_m}}}$, $\overline{\delta_{\mathrm{cm_m}}}$ and $\overline{\gamma_{\mathrm{cm_m}}}$ with $\arg(S_{\mathrm{HH}} + S_{\mathrm{VV}})$, $\arg(S_{\mathrm{HH}} - S_{\mathrm{VV}})$ and $\arg(S_{\mathrm{HV}})$, respectively. The correlation coefficients in Fig. 8(a-2), (b-2) and (c-2) are 0.70, 0.70, and 0.71, respectively. Those in Fig. 9(a-2), (b-2) and (c-2) are 0.67, 0.66, and 0.67, respectively. Those in Fig. 10(a-2), (b-2) and (c-2) are 0.70, 0.68 and 0.68, respectively. There are also high correlations in these diagrams.

V. Discussions

We find from the discussions below that the main origins that cause SPs are scattering itself and the interference of waves from multiple scattering sources.

A. First Main Origin of SPs: Scattering

Fig. 11 shows the relationship between the changes in polarization and those in phase in the processing. The results

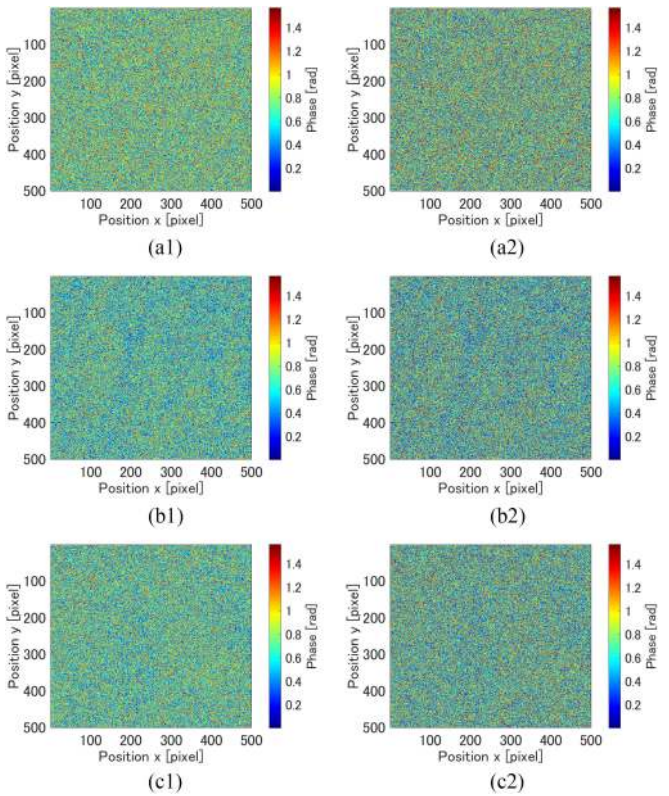

Fig. 6. (⋆-1) $\overline{\beta_{\mathrm{cm_m}}}$ map in the Pauli coherency matrix and (⋆-2) $\beta_{\mathrm{opt_m}}$ map of $\boldsymbol{w}_{\mathrm{opt_m}}$ in PPO-BD for the areas of (a-⋆) Forest, (b-⋆) Grassland, and (c-⋆) Scree.

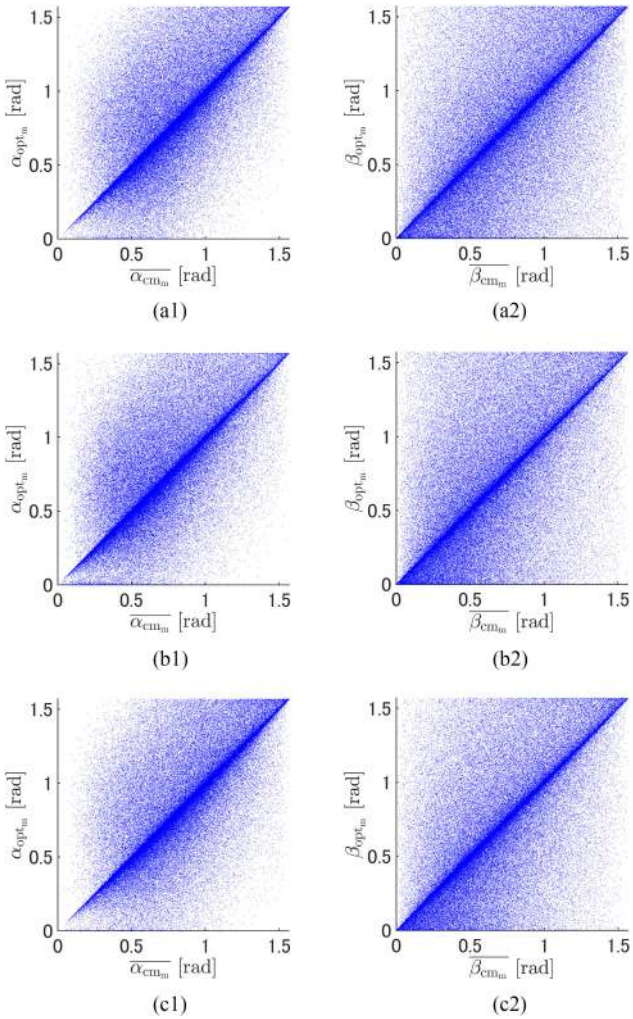

Fig. 7. Scatter diagrams of ($\star$-1) $\overline{\alpha_{\mathrm{cm_m}}}$ and $\alpha_{\mathrm{opt_m}}$, and ($\star$-2) $\overline{\beta_{\mathrm{cm_m}}}$ and $\beta_{\mathrm{opt_m}}$ for the areas of (a-$\star$) Forest, (b-$\star$) Grassland and (c-$\star$) Scree.

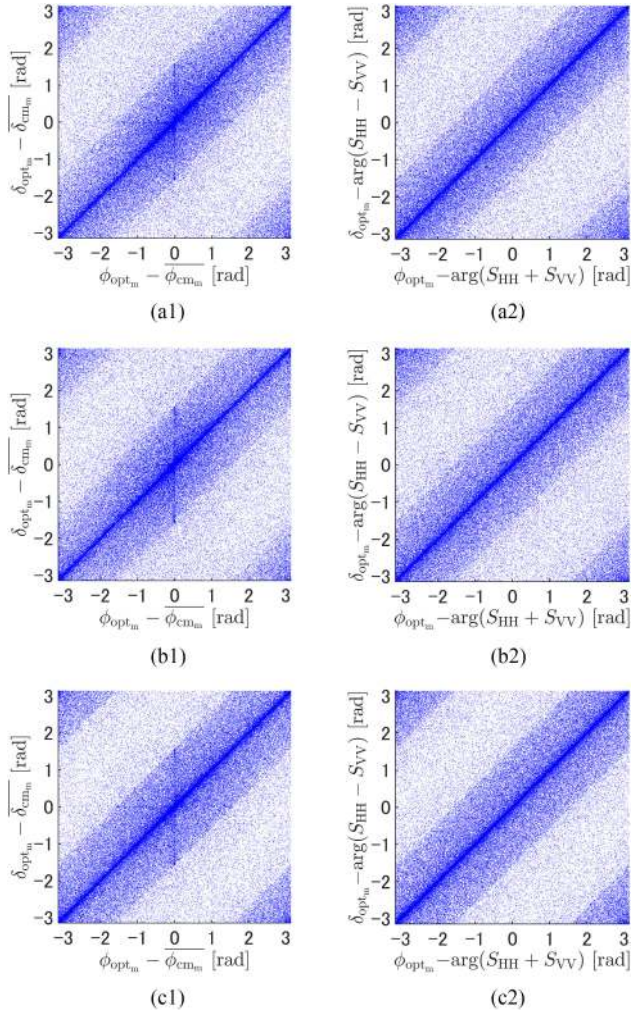

Fig. 8. Scatter diagrams of ($\star$-1) $\phi_{\mathrm{opt_m}} - \overline{\phi_{\mathrm{cm_m}}}$ and $\delta_{\mathrm{opt_m}} - \overline{\delta_{\mathrm{cm_m}}}$, and ($\star$-2) $\phi_{\mathrm{opt_m}} - \arg(S_{\mathrm{HH}} + S_{\mathrm{VV}})$ and $\delta_{\mathrm{opt_m}} - \arg(S_{\mathrm{HH}} - S_{\mathrm{VV}})$ for the areas of (a-$\star$) Forest, (b-$\star$) Grassland and (c-$\star$) Scree.

of the analysis show that there is a high correlation between the parameters in the Pauli coherency matrix and those in the scattering mechanism vector optimized by PPO-BD. The parameters in the Pauli coherency matrix and the same parameters in $\boldsymbol{w}_{\mathrm{opt_m}}$ of PPO-BD represent polarization changes and phase changes, respectively. It means that there is a correlation between polarization changes and phase changes. In other words, the changes in polarization and those in phase are caused by an identical phenomenon, namely, scattering itself. Therefore, scattering itself is one of the main origins that cause SPs.

B. Second Main Origin of SPs: The Interference of Waves Coming From Multiple Scattering Sources

Fig. 12(a) shows the histogram of the difference between $\overline{\phi_{\mathrm{opt_m}}} - \arg(S_{\mathrm{HH}} + S_{\mathrm{VV}})$ and $\overline{\delta_{\mathrm{opt_m}}} - \arg(S_{\mathrm{HH}} - S_{\mathrm{VV}})$ while (b) presents the identical histogram enlarged in the vertical direction. The central peak represents the pixels where the optimization by PPO-BD succeeded, that is, where scattering caused SPs. We can fit the bulge of the peak by the Laplace distribution (the double exponential distribution). The probability density function $f(x)$ of the Laplace distribution is given by

$$f(x) = \frac{1}{2\phi} \exp\left(-\frac{|x-\mu|}{\phi}\right) \tag{19}$$

where the mean and the variance are μ and $2\phi^2$, respectively. Fig. 12(a) and (b) show also the fitting curves assuming the Laplace distribution. Since the exponential distribution has the memoryless property, this result suggests that another one of the main origins of SPs is the interference of waves from multiple scattering sources independent of one another. The differences between the histogram and the fitting curve are attributed to the angle representation folded into $[-\pi/2, \pi/2]$.

C. Other Origins

We can find that the pixel number is flat in $[-\pi, -\pi/2]$ and $[\pi/2, \pi]$, which shows another origin having a uniform distribution over $[-\pi, \pi]$. It should be thermal noise. As a whole, the contributions of scattering, interference and thermal noise are 54 : 31 : 15 according to the pixel counts in Fig. 12(a).

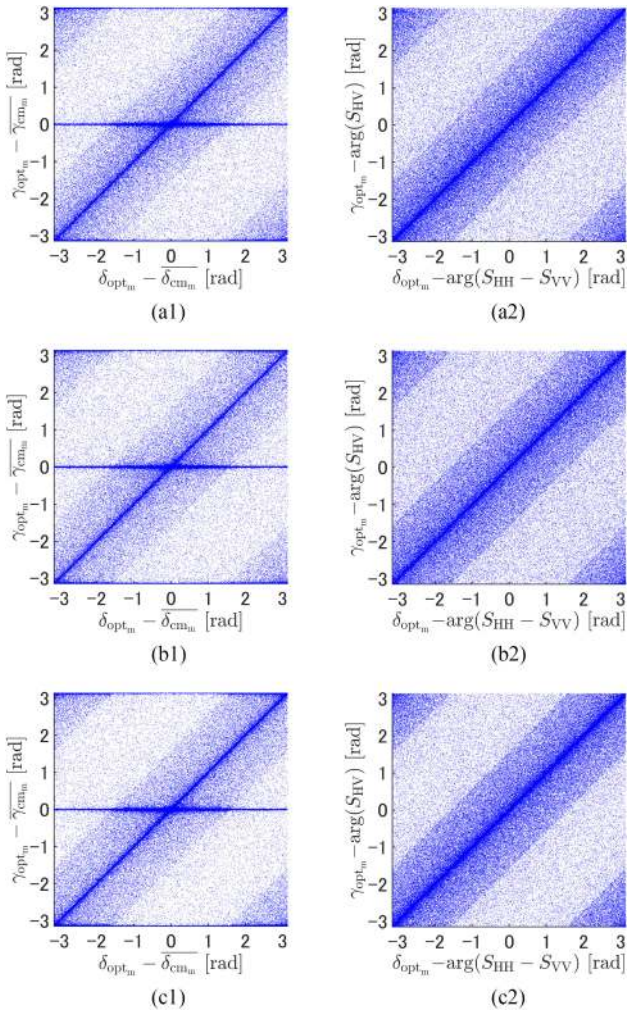

Fig. 9. Scatter diagrams of ($\star$-1) $\delta_{\mathrm{opt_m}} - \overline{\delta_{\mathrm{cm_m}}}$ and $\gamma_{\mathrm{opt_m}} - \overline{\gamma_{\mathrm{cm_m}}}$, and ($\star$-2) $\delta_{\mathrm{opt_m}} - \arg(S_{\mathrm{HH}} - S_{\mathrm{VV}})$ and $\gamma_{\mathrm{opt_m}} - \arg(S_{\mathrm{HV}})$ for the areas of (a-$\star$) Forest, (b-$\star$) Grassland and (c-$\star$) Scree.

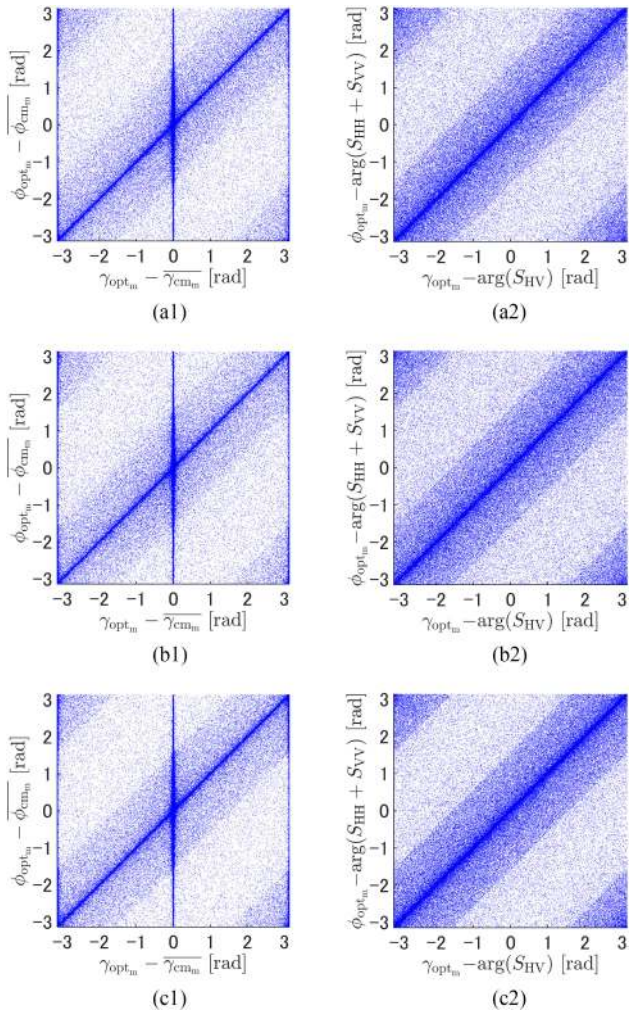

Fig. 10. Scatter diagrams of ($\star$-1) $\gamma_{\mathrm{opt_m}} - \overline{\gamma_{\mathrm{cm_m}}}$ and $\phi_{\mathrm{opt_m}} - \overline{\phi_{\mathrm{cm_m}}}$, and ($\star$-2) $\gamma_{\mathrm{opt_m}} - \arg(S_{\mathrm{HV}})$ and $\phi_{\mathrm{opt_m}} - \arg(S_{\mathrm{HH}} + S_{\mathrm{VV}})$ for the areas of (a-$\star$) Forest, (b-$\star$) Grassland and (c-$\star$) Scree.

The factors shown above cause the phase changes. Scattering is always the factor of SPs. In addition, interference and white noise have influence in a part of pixels. Fig. 12 shows that the factors are summed up in such a manner.

D. Compensation of Polarimetric Changes in the PPO-BD Optimization

1) Proposal of Scattering Sphere: In the last section, we found that scattering is one of the main origins of SPs. In this section, we examine how the PPO-BD optimization compensates the polarimetric changes caused by scattering. For this purpose, we need a new form to express polarimetric features of scattering mechanisms. Instead of the Poincare sphere, which is used to represent polarization, we propose a sphere that represents the features of scatterers visually. We name it "scattering sphere".

Fig. 13 shows the scattering sphere, where the coordinates represent the absolute values of $k_1 = S_{\mathrm{HH}} + S_{\mathrm{VV}}, k_2 = S_{\mathrm{HH}} - S_{\mathrm{VV}}$ and $k_3 = 2S_{\mathrm{HV}}$, respectively. The angle between $|k_1|$ axis and the radius vector projected on $|k_1| - |k_2|$ plane represents angle $\overline{\alpha_{\mathrm{cm_m}}}$ while the angle between $|k_1| - |k_2|$ plane and the radius vector represents angle $\overline{\beta_{\mathrm{cm_m}}}$. Fig. 13 also shows the scattering mechanisms of representative points.

2) Experiments and Results: We use the ALOS-2 data that was used in Section IV. We plot the scattering states on the scattering sphere for the areas of Field, Town, Forest and Lake We chose three 100×100-pixel sample areas for each land cover class by considering the heterogeneity [34], [35]. Fig. 3 shows the sample areas.

The scattering vector after PPO-BD optimization is given by calculating the Hadamard product of the scattering vector and the complex conjugate of the optimized scattering mechanism vector $\boldsymbol{w}_{\mathrm{opt}}$ as

$$\boldsymbol{k}_{\mathrm{opt}} = \overline{\boldsymbol{w}_{\mathrm{opt}}} \odot \boldsymbol{k}. \tag{20}$$

Fig. 14 shows the scattering spheres for the areas of Field1, Field2 and Field3. In the plots, we find that there are more points around (1, 0, 0) after the PPO-BD than before PPO-BD. Since surface scattering is dominant in a field, it means that PPO-BD optimization enhances the actual surface scattering mechanisms. Fig. 15 shows the scattering spheres for the areas of Town1,

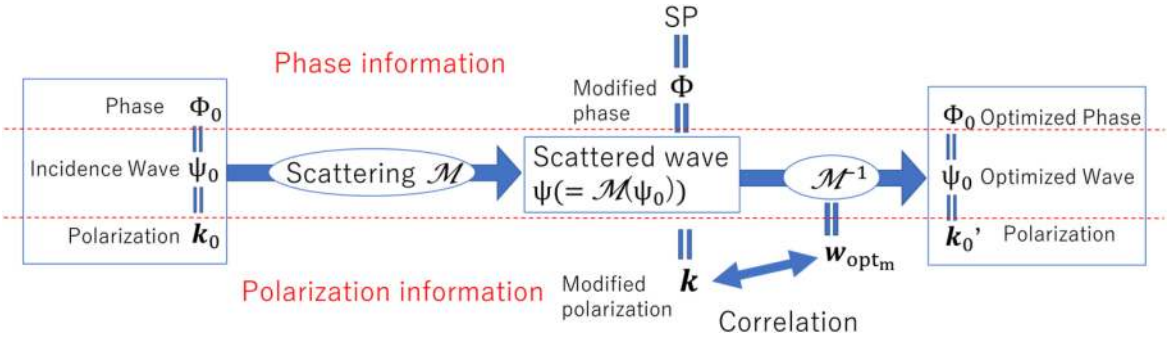

Fig. 11. Scattering and optimization processes, and the relationship between the changes in polarization and phase.

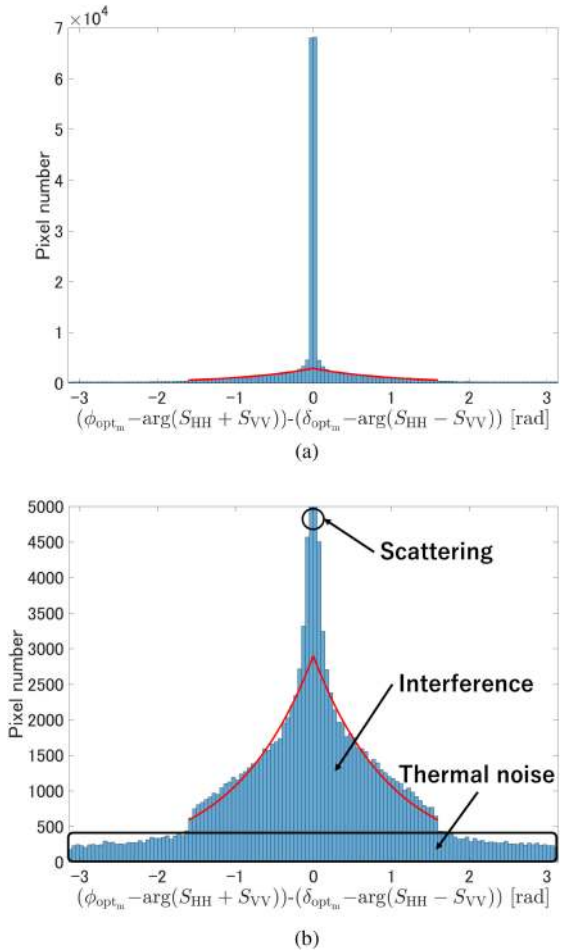

Fig. 12. (a) Histogram of the differences between $\phi_{\mathrm{opt_m}}-\arg(S_{\mathrm{HH}}+S_{\mathrm{VV}})$ and $\delta_{\mathrm{opt_m}}-\arg(S_{\mathrm{HH}}-S_{\mathrm{VV}})$ for the area of Forest fitted by the Laplace distribution ($\phi = 1.0043$) and (b) vertically enlarged one.

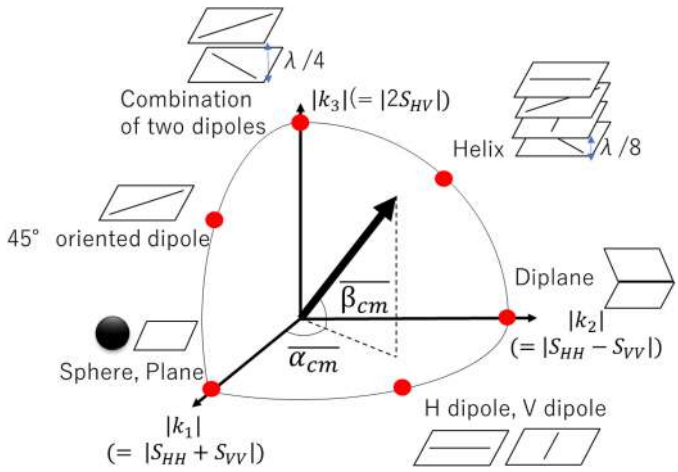

Fig. 13. Scattering sphere (1/8 sphere) and the scatterers corresponding to the representative points.

Town2, and Town3. Since double bounce scattering is dominant in town, we find that there are more points around (0, 1, 0) than other areas. This tendency increases after PPO-BD optimization.

Fig. 16 shows the scattering spheres for the areas of Forest1, Forest2 and Forest3. Since volume scattering is dominant in forest, we find that most of the points are situated around the central area. These points spread on the sphere after PPO-BD optimization. Fig. 17 shows the scattering spheres for the areas of Lake1, Lake2, and Lake3. Since the water surface causes the specular reflection, the data mostly originate from noise. Therefore, we find that most of the points are situated around the central area. We also find in all the areas that the plot after the PPO-BD optimization shows a wider distribution than those before PPO-BD. This result shows that PPO-BD emphasizes the respective features of the scattering mechanisms.

Figs. 18–20 show the histograms of $|k_1|$, $|k_2|$ and $|k_3|$ in Figs. 14–17. The peak values of the histograms after PPO-BD optimization (solid curves) are lower than those before PPO-BD (dashed curves), while the values at the skirts after PPO-BD optimization are higher than those before PPO-BD. That is, that PPO-BD reduces randomness in the polarimetric features, and enhances the polarimetric features specific to deterministic scattering such as surface and double-bounce scattering. It means that the PPO-BD optimization reduces SPs by decreasing probabilistic/random scattering mechanisms. These results show that SPs are caused by probabilistic/random scattering mechanisms other than deterministic scattering such as surface and double-bounce scattering.

Fig. 21 shows the process of SP generation caused by probabilistic/random scattering. In deterministic scattering such as surface and double-bounce scattering, the scattering process of each pixel in the master image will be identical with that in the

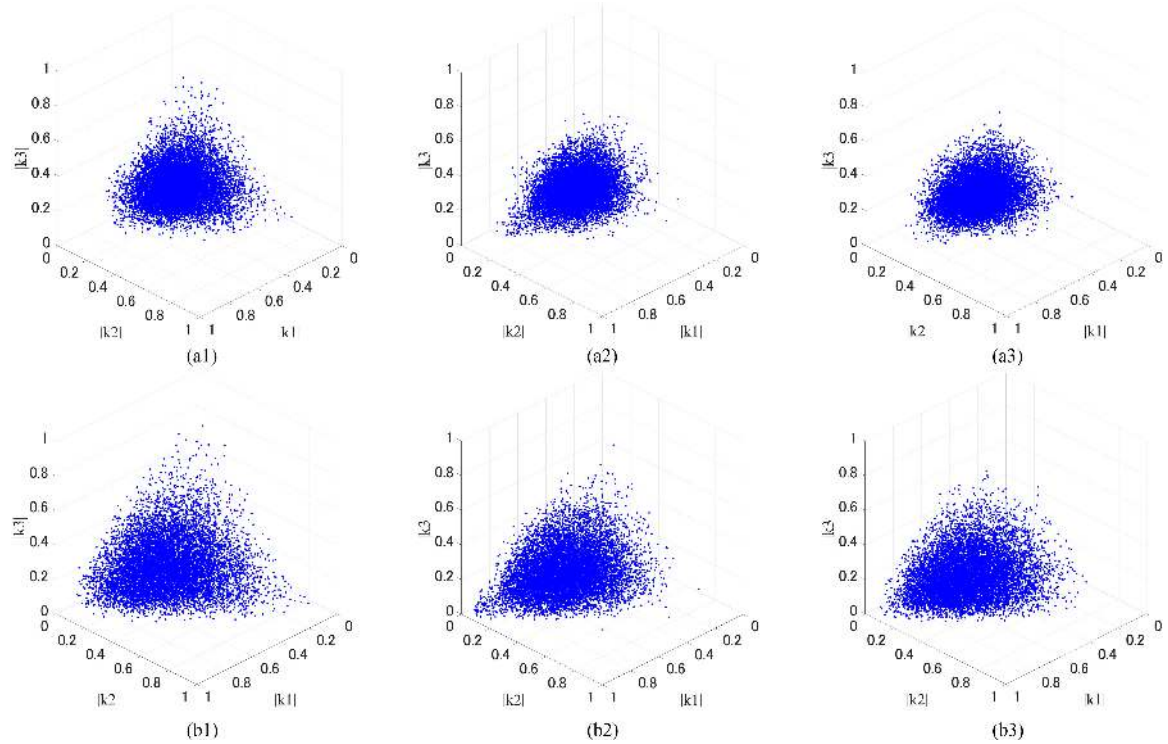

Fig. 14. Scattering spheres (a-⋆) before and (b-⋆) after PPO-BD treatment for the areas of (⋆-1) Field1, (⋆-2) Field2, and (⋆-3) Field3.

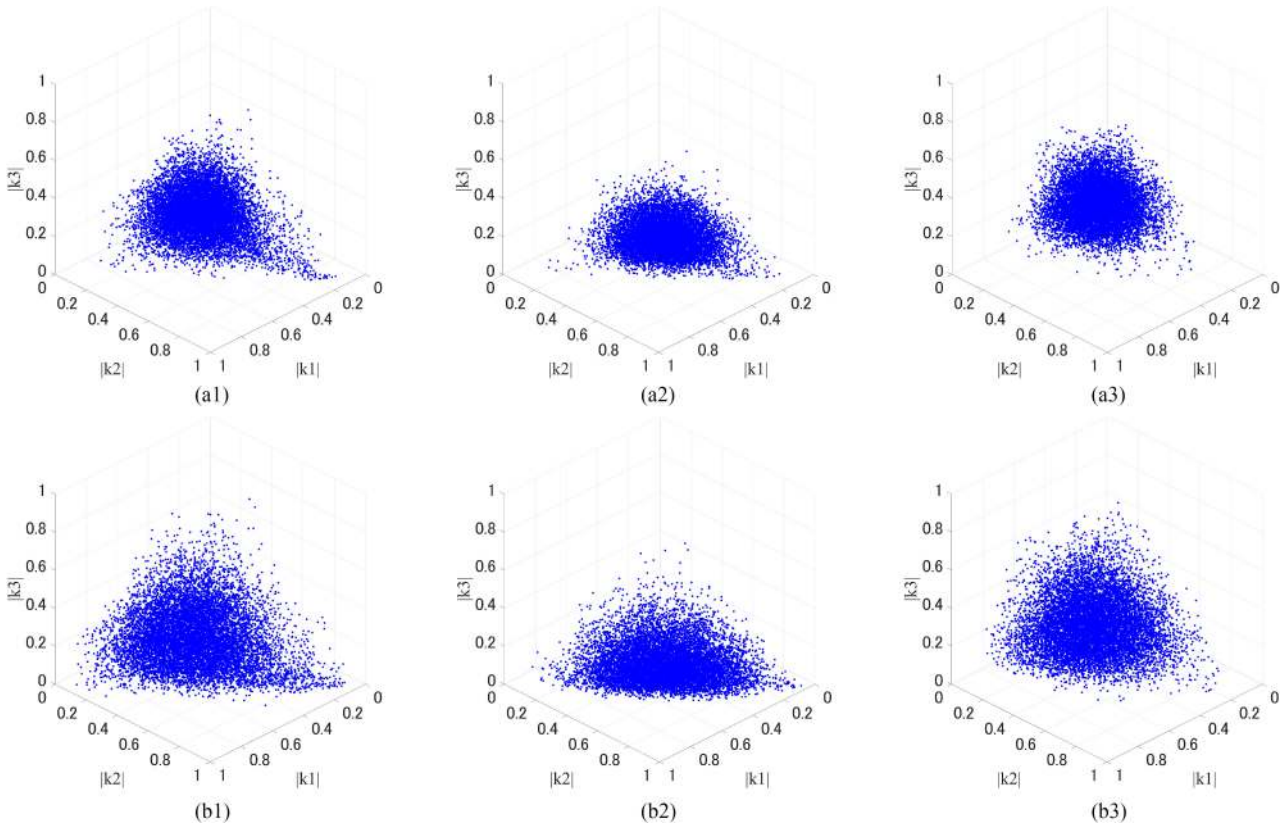

Fig. 15. Scattering spheres (a-⋆) before and (b-⋆) after PPO-BD treatment for the areas of (⋆-1) Town1, (⋆-2) Town2, and (⋆-3) Town3.

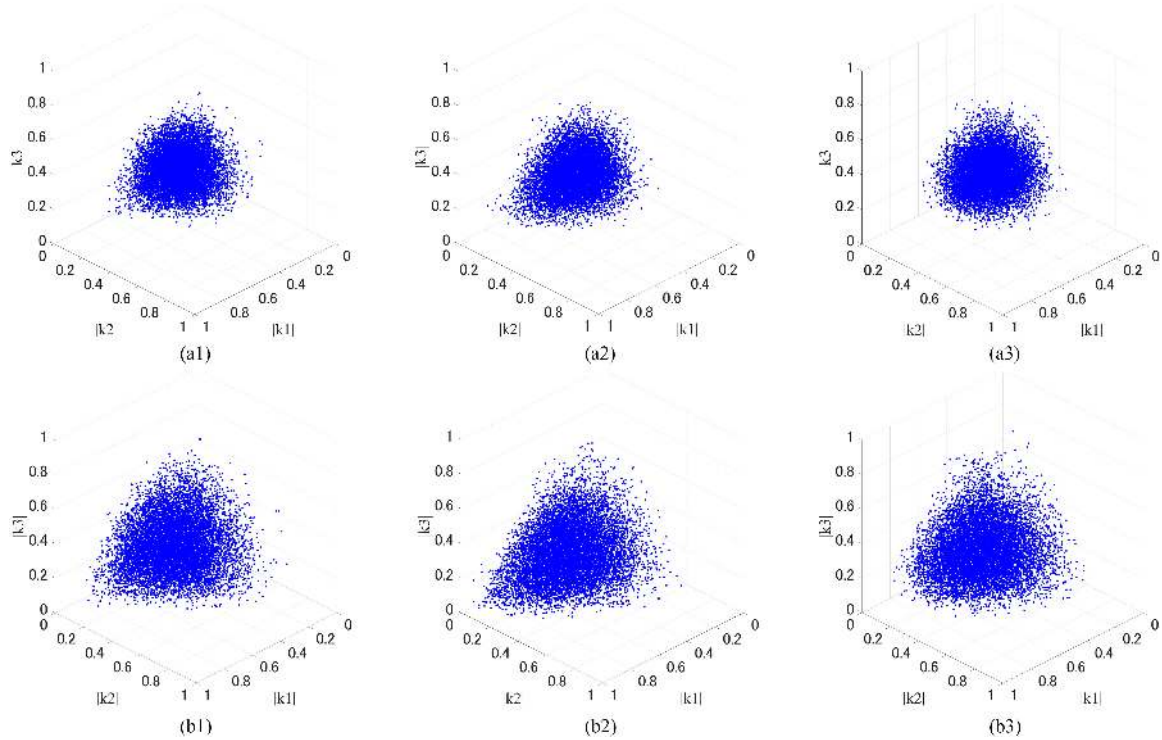

Fig. 16. Scattering spheres (a-⋆) before and (b-⋆) after PPO-BD treatment for the areas of (⋆-1) Forest1, (⋆-2) Forest2, and (⋆-3) Forest3.

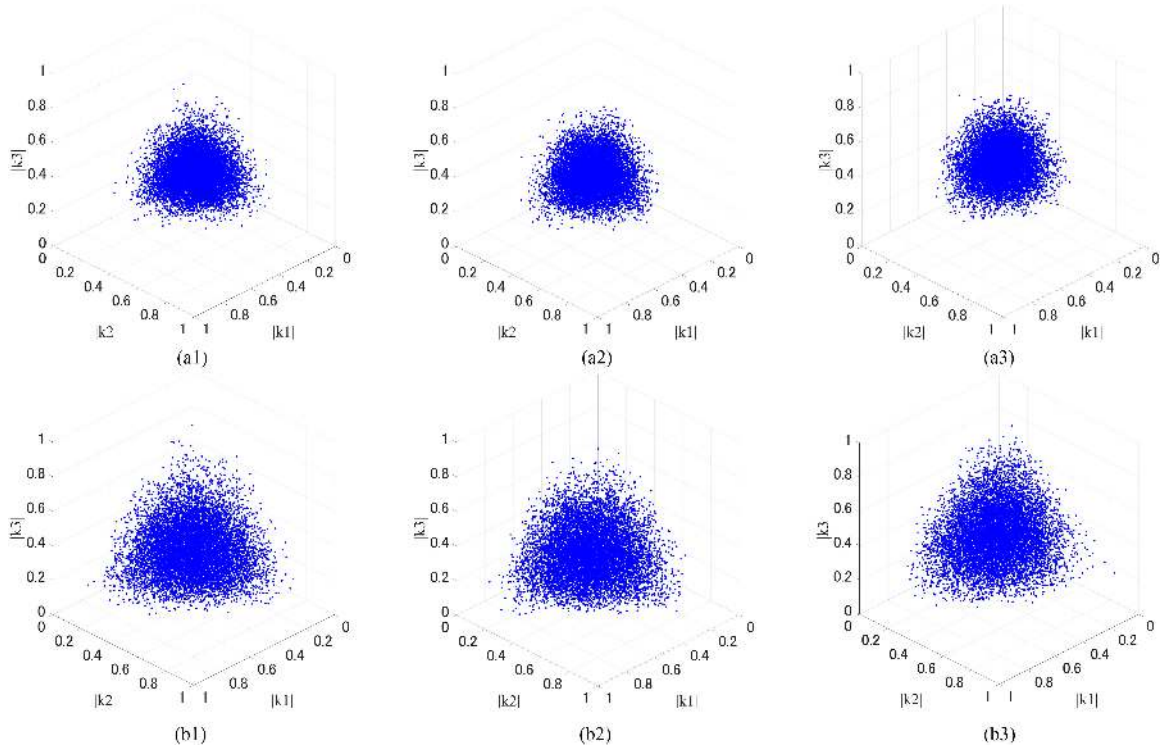

Fig. 17. Scattering spheres (a-⋆) before and (b-⋆) after PPO-BD treatment for the areas of (⋆-1) Lake1, (⋆-2) Lake2, and (⋆-3) Lake3.

slave image. Therefore, the phase changes caused by scattering is mostly canceled through the interference processing. But, in probabilistic/random scattering such as volume scattering, the scattering processes can be different from each other due to the difference of the incident angles, the effect of the wind, the growth of the plants and so on and so forth. Thus, the phase changes cannot be canceled, which leads to SP generation. Therefore, by investigating the deterministic scattering mechanism in the area, we can know that the other probabilistic/random scattering mechanisms are the cause of SPs.

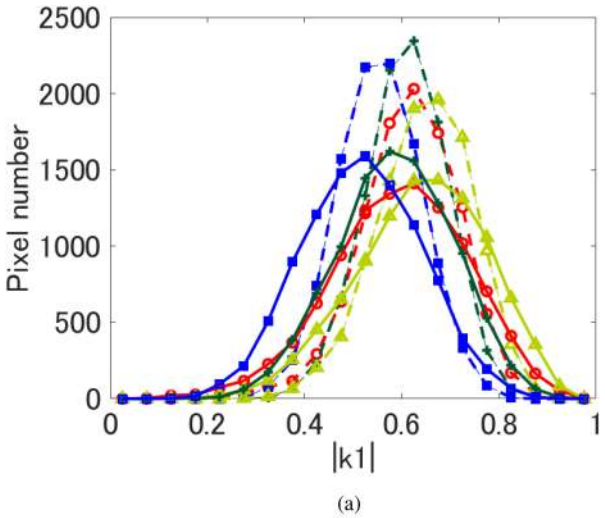

(a)

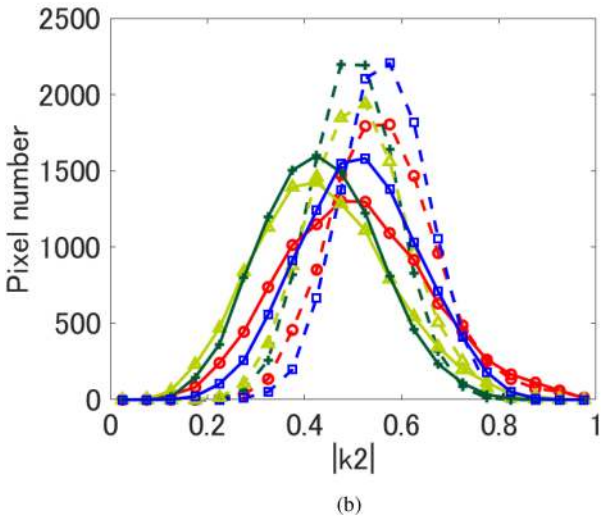

(b)

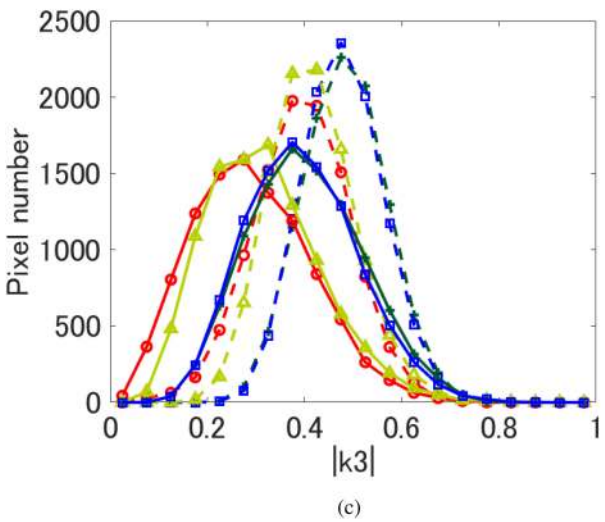

(c)

Fig. 18. Histograms of (a) $|k_1|$, (b) $|k_2|$, and (c) $|k_3|$ before (dashed curves) and after (solid curves) PPO-BD treatment (Yellow green: Field1, Red: Town1, Dark green: Forest1, Blue: Lake1).

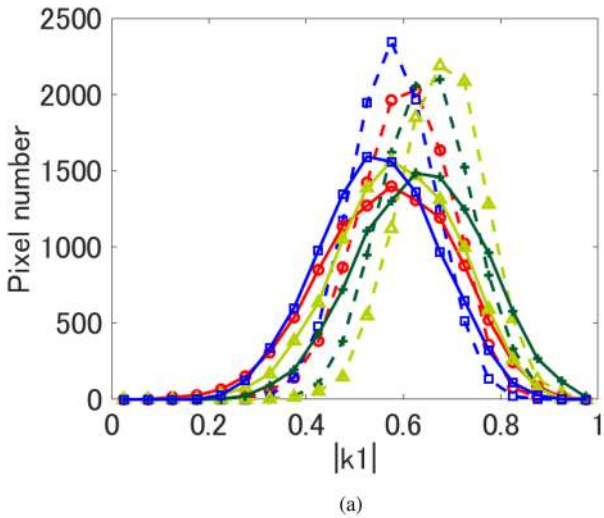

(a)

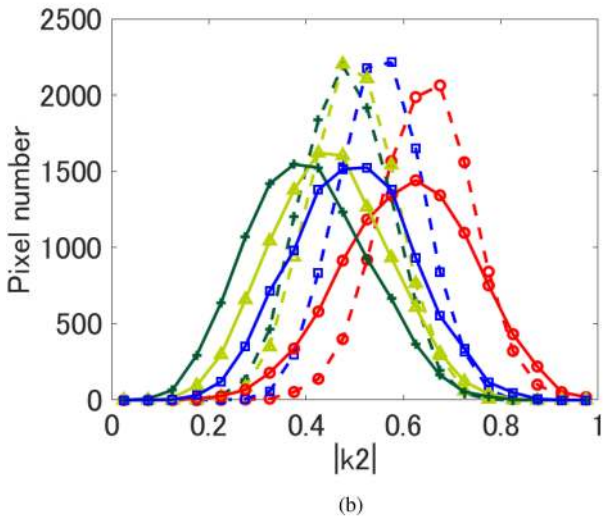

(b)

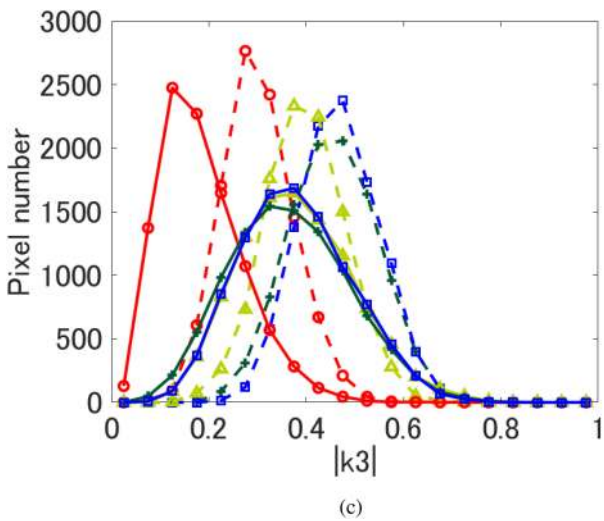

(c)

Fig. 19. Histograms of (a) $|k_1|$, (b) $|k_2|$, and (c) $|k_3|$ before (dashed curves) and after (solid curves) PPO-BD treatment (Yellow green: Field2, Red: Town2, Dark green: Forest2, Blue: Lake2).

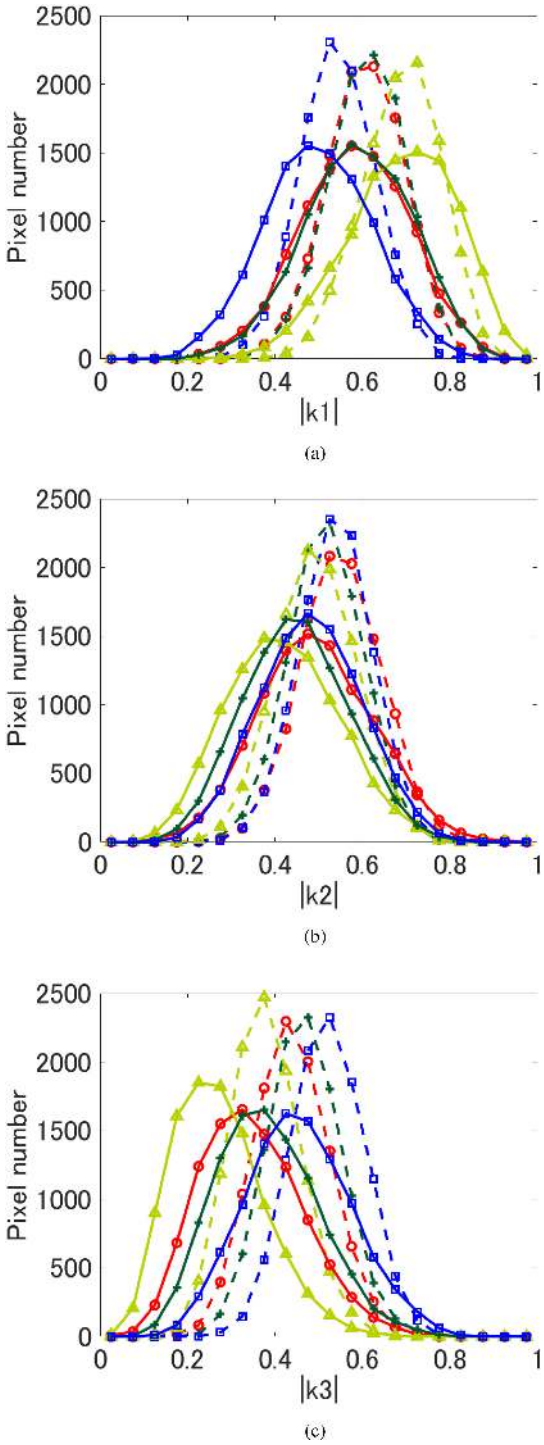

Fig. 20. Histograms of (a) $|k_1|$, (b) $|k_2|$, and (c) $|k_3|$ before (dashed curves) and after (solid curves) PPO-BD treatment (Yellow green: Field3, Red: Town3, Dark green: Forest3, Blue: Lake3).

We also investigate the scattering coefficients of each polarization before and after PPO-BD optimization to find out which polarization contributes to the highly-accurate DEM generation most. Table I shows the scattering coefficients of each polarization before and after PPO-BD optimization for the areas of Forest, Grassland and Scree. The coefficients after PPO-BD are calculated for obtained k_{opt} values backward in (3) and (20).

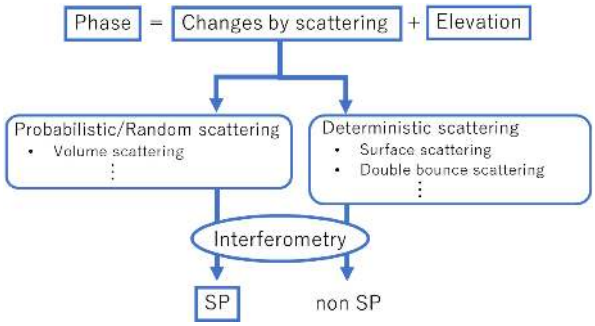

Fig. 21. Diagram summarizing SP generation mechanism showing that SPs are caused by the probabilistic scattering.

TABLE I
SCATTERING COEFFICIENTS OF EACH POLARIZATION BEFORE AND AFTER PPO-BD OPTIMIZATION

Land cover	Polarization	Original scattering coefficient [$\times 10^4$]	Scattering coefficient calculated backward from k_{opt}[$\times 10^4$]
Forest	$\lvert S_{\mathrm{HH}}\rvert$	25.8	13.8
	$\lvert S_{\mathrm{HV}}\rvert$	13.6	7.1
	$\lvert S_{\mathrm{VV}}\rvert$	25.3	22.3
Field	$\lvert S_{\mathrm{HH}}\rvert$	11.9	7.0
	$\lvert S_{\mathrm{HV}}\rvert$	4.8	2.2
	$\lvert S_{\mathrm{VV}}\rvert$	11.7	10.7
Scree	$\lvert S_{\mathrm{HH}}\rvert$	6.7	3.8
	$\lvert S_{\mathrm{HV}}\rvert$	3.6	2.8
	$\lvert S_{\mathrm{VV}}\rvert$	7.2	6.1

In all the areas, the scattering coefficients of VV polarization have the highest scattering coefficients and HV polarization has the lowest scattering coefficients. Therefore, VV polarization contributes to the highly-accurate DEM generation best while HH does secondly. This result means that we can generate the most accurate DEMs by full-pol data, and that in the case of two polarization combinations, HH/VV first, VV/HV secondly and HH/HV thirdly work for the highly-accurate DEM generation.

VI. CONCLUSION

In this article, we investigated the relationship between the polarization states and the phase distortion in PolInSAR to elucidate the generation mechanisms of SPs. We found that there is a high correlation between the parameters in the Pauli coherency matrix and those in the scattering mechanism vector optimized by the PPO-BD method. It means that there is a correlation between the parameters of polarization and those of the phase compensation in the PPO-BD optimization. In other words, the main changes in phase and those in polarization are caused by an identical phenomenon, that is, scattering itself. Therefore, we can use the parameters of polarization to reduce SPs. We also found that another one of the main origins of SPs is the interference of waves from multiple scattering sources. Lastly, we examined how the PPO-BD optimization compensates polarization changes caused by scattering by introducing the scattering sphere. We found that PPO-BD reduces randomness and enhances the polarimetric features specific to deterministic scattering such as surface and double-bounce scattering. It means that probabilistic/random scattering mechanisms are the main origin of SP generation.

ACKNOWLEDGMENT

The ALOS-2 original data are copyrighted by Japan Aerospace Exploration Agency (JAXA) and provided under JAXA 4th ALOS Research Announcement PI No. 1154.

REFERENCES

[1] W.-M. Boerner, "Recent advances in extra-wide-band polarimetry, interferometry and polarimetric interferometry in synthetic aperture remote sensing and its applications," *Proc. Inst. Elect. Eng.—Radar, Sonar, Navig.*, vol. 150, no. 3, pp. 113–124, 2003.

[2] K. Ouchi, *Principles of Synthetic Aperture Radar for Remote Sensing*. Tokyo, Japan: Tokyo Denki Univ. Press, 2004.

[3] D. C. Ghiglia and M. D. Pritt, *Two-Dimensional Phase Unwrapping: Theory, Algorithms, and Software*. New York, NY, USA: Wiley, 1998, vol. 4.

[4] M. Costantini, "A novel phase unwrapping method based on network programming," *IEEE Trans. Geosci. Remote Sens.*, vol. 36, no. 3, pp. 813–821, May 1998.

[5] M. D. Pritt and J. S. Shipman, "Least-squares two-dimensional phase unwrapping using FFT's," *IEEE Trans. Geosci. Remote Sens.*, vol. 32, no. 3, pp. 706–708, May 1994.

[6] G. Fornaro, G. Franceschetti, and R. Lanari, "Interferometric SAR phase unwrapping using green's formulation," *IEEE Trans. Geosci. Remote Sens.*, vol. 34, no. 3, pp. 720–727, May 1996.

[7] A. Reigber and J. Moreira, "Phase unwrapping by fusion of local and global methods," in *Proc. IEEE Int. Geosci. Remote Sens. Symp., Singapore*, 1997, vol. 2., pp. 869–871.

[8] F. Lombardini, "Optimum absolute phase retrieval in three-element SAR interferometer," *Electron. Lett.*, vol. 34, no. 15, pp. 1522–1524, 1998.

[9] A. B. Suksmono and A. Hirose, "Progressive transform-based phase unwrapping utilizing a recursive structure," *IEICE Trans. Commun.*, vol. 89, no. 3, pp. 929–936, 2006.

[10] A. Pepe and R. Lanari, "On the extension of the minimum cost flow algorithm for phase unwrapping of multitemporal differential SAR interferograms," *IEEE Trans. Geosci. Remote Sens.*, vol. 44, no. 9, pp. 2374–2383, Sep. 2006.

[11] R. M. Goldstein and C. L. Werner, "Radar interferogram filtering for geophysical applications," *Geophys. Res. Lett.*, vol. 25, no. 21, pp. 4035–4038, 1998.

[12] J.-S. Lee, K. P. Papathanassiou, T. L. Ainsworth, M. R. Grunes, and A. Reigber, "A new technique for noise filtering of SAR interferometric phase images," *IEEE Trans. Geosci. Remote Sens.*, vol. 36, no. 5, pp. 1456–1465, Sep. 1998.

[13] A. B. Suksmono and A. Hirose, "Adaptive noise reduction of InSAR images based on a complex-valued MRF model and its application to phase unwrapping problem," *IEEE Trans. Geosci. Remote Sens.*, vol. 40, no. 3, pp. 699–709, Mar. 2002.

[14] A. B. Suksmono and A. Hirose, "Interferometric SAR image restoration using monte carlo metropolis method," *IEEE Trans. Signal Process.*, vol. 50, no. 2, pp. 290–298, Feb. 2002.

[15] G. Ferraiuolo and G. Poggi, "A Bayesian filtering technique for SAR interferometric phase fields," *IEEE Trans. Image Process.*, vol. 13, no. 10, pp. 1368–1378, Oct. 2004.

[16] R. Yamaki and A. Hirose, "Singular unit restoration in interferograms based on complex-valued Markov random field model for phase unwrapping," *IEEE Geosci. Remote Sens. Lett.*, vol. 6, no. 1, pp. 18–22, Jan. 2009.

[17] H. Huang and Q. Wang, "A method of filtering and unwrapping SAR interferometric phase based on nonlinear phase model," *Prog. Electromagn. Res.*, vol. 144, pp. 67–78, 2014.

[18] R. Natsuaki and A. Hirose, "SPEC methoda fine coregistration method for SAR interferometry," *IEEE Trans. Geosci. Remote Sens.*, vol. 49, no. 1, pp. 28–37, Jan. 2011.

[19] R. Natsuaki and A. Hirose, "InSAR local co-registration method assisted by shape-from-shading," *IEEE J. Sel. Topics Appl. Earth Observ. Remote Sens.*, vol. 6, no. 2, pp. 953–959, Apr. 2013.

[20] J. Ma, J. C.-W. Chan, and F. Canters, "Fully automatic subpixel image registration of multiangle CHRIS/Proba data," *IEEE Trans. Geosci. Remote Sens.*, vol. 48, no. 7, pp. 2829–2839, Jul. 2010.

[21] E. Sansosti, P. Berardino, M. Manunta, F. Serafino, and G. Fornaro, "Geometrical SAR image registration," *IEEE Trans. Geosci. Remote Sens.*, vol. 44, no. 10, pp. 2861–2870, Oct. 2006.

[22] K. P. Papathanassiou and S. R. Cloude, "Single-baseline polarimetric SAR interferometry," *IEEE Trans. Geosci. Remote Sens.*, vol. 39, no. 11, pp. 2352–2363, Nov. 2001.

[23] X. Li, H. Guo, C. Wang, Z. Li, and J. Liao, "Generation and error analysis of DEM using spaceborne polarimetric SAR interferometry data," in *Proc. IEEE Int. Geosci. Remote Sens. Symp. , Toronto*, 2002, vol. 5., pp. 2705–2707.

[24] M. Brandfass, "Generation of bald earth digital elevation models as applied to polarimetric SAR interferometry," in *Proc. IEEE Int. Geosci. Remote Sens. Symp.*, 2002, vol. 2., pp. 1014–1016.

[25] E. Colin, C. Titin-Schnaider, and W. Tabbara, "An interferometric coherence optimization method in radar polarimetry for high-resolution imagery," *IEEE Trans. Geosci. Remote Sens.*, vol. 44, no. 1, pp. 167–175, Jan. 2006.

[26] W. Zhou, E. Chen, G. Liu, W. Li, Q. Feng, and X. Wang, "Polarimetric interferometic coherence optimization based DEM extraction method for ALOS PALSAR data," in *Proc. IEEE Int. Geosci. Remote Sens. Symp., Munich*, 2012, pp. 2691–2694.

[27] T. Shimada, R. Natsuaki, and A. Hirose, "Pixel-by-pixel scattering mechanism vector optimization in high-resolution PolInSAR," *IEEE Trans. Geosci. Remote Sens.*, vol. 56, no. 5, pp. 2587–2596, May 2018.

[28] T. Shimada and A. Hirose, "Proposal of pixel-by-pixel optimization of scattering mechanism vectors in PolInSAR to generate accurate digital elevation model," in *Proc. IEEE Int. Geosci. Remote Sens. Symp., Fortworth*, 2017, pp. 83–86.

[29] S. Fujinami, R. Natsuaki, and A. Hirose, "Experimental analysis of singular point generation mechanisms in interferometric SAR using optics: The possibility of singular point generation by interference in a single pixel," in *Proc. IEEE Int. Geosci. Remote Sens. Symp., Milan*, 2015, pp. 4256–4259.

[30] S. Fujinami, R. Natsuaki, K. Ichikawa, and A. Hirose, "Experimental analysis on the mechanisms of singular point generation in InSAR by employing scaled optical interferometry," *IEEE Trans. Geosci. Remote Sens.*, vol. 56, no. 7, pp. 3830–3837, Jul. 2018.

[31] R. M. Goldstein, H. A. Zebker, and C. L. Werner, "Satellite radar interferometry: Two-dimensional phase unwrapping," *Radio Sci.*, vol. 23, no. 4, pp. 713–720, 1988.

[32] S. R. Cloude and K. P. Papathanassiou, "Polarimetric SAR interferometry," *IEEE Trans. Geosci. Remote Sens.*, vol. 36, no. 5, pp. 1551–1565, Sep. 1998.

[33] M. Tabb, J. Orrey, T. Flynn, and R. Carande, "Phase diversity: A decomposition for vegetation parameter estimation using polarimetric SAR interferometry," in *Proc. Eur. Conf. Synthetic Aperture Radar, Cologne*, 2002, vol. 2, pp. 721–724.

[34] S. Chauhan, H. S. Srivastava, and P. Patel, "Wheat crop biophysical parameters retrieval using hybrid-polarized RISAT-1 SAR data," *Remote Sens. Environ.*, vol. 216, pp. 28–43, 2018.

[35] P. Patel, H. S. Srivastava, and R. R. Navalgund, "Use of synthetic aperture radar polarimetry to characterize wetland targets of Keoladeo National Park, Bharatpur, India," *Current Sci.*, vol. 97, no. 4, pp. 529–537, 2009.

Yuta Otsuka received the B.S. and M.S. degrees in electrical engineering and information systems from The University of Tokyo, Tokyo, Japan, in 2018 and 2020, respectively.

His research interests include phase unwrapping and synthetic aperture radar interferometry.

Tomoharu Shimada received the B.S. and M.S. degrees in electrical engineering and information systems from The University of Tokyo, Tokyo, Japan, in 2015 and 2017, respectively.

He is currently with Fujifilm, Tokyo. His research interests include phase unwrapping and synthetic aperture radar interferometry.

Ryo Natsuaki (Member, IEEE) received B. S., M. S., and Ph. D. degrees in electrical engineering from The University of Tokyo, Japan in 2009, 2011, and 2014, respectively.

He was an Aerospace Project Research Associate of Japan Aerospace Exploration Agency (JAXA) from 2014 to 2017. He is currently a Lecturer with the Department of Electrical Engineering and Information Systems, The University of Tokyo. He is also a Guest Scientist with Microwaves and Radar Institute, German Aerospace Center (DLR) from 2018 to 2020 under JSPS Overseas Research Fellowships. His research interests include active remote sensing with synthetic aperture radar (SAR).

He is a member of IEEE Geoscience and Remote Sensing Society (GRSS) and the Institute of Electronics, Information and Communication Engineers (IEICE). He currently serves as an Assistant Secretary of IEICE technical committee on Space, Aeronautical and Navigational Electronics (SANE) and a Publicity Chair of IEEE International Geoscience and Remote Sensing Symposium (IGARSS).

Akira Hirose (Fellow, IEEE) received the Ph.D. degree in electronic engineering from The University of Tokyo, in 1991.

He is currently a Professor with the Department of Electrical Engineering and Information Systems, University of Tokyo. The main fields of his research interests are wireless electronics and neural networks.

He had served as a President of the Japanese Neural Network Society (JNNS) from 2013 to 2015, President of Asia-Pacific Neural Network Society (APNNS), in 2016, Vice President of the Institute of Electronics, Information and Communication Engineers (IEICE) Electronics Society from 2013 to 2015, Editor-in-Chief of the IEICE Transactions on Electronics from 2011 to 2012, Associate Editor of journals such as IEEE Transactions on Neural Networks from 2009 to 2011, IEEE Geoscience and Remote Sensing Newsletter from 2009 to 2012, as well as General Chair of Asia-Pacific Conference on Synthetic Aperture Radar (APSAR) 2013 Tsukuba, General Chair of International Conference on Neural Information Processing (ICONIP) 2016 Kyoto, and General Chair of International Geoscience and Remote Sensing Symposium (IGARSS) 2019 Yokohama. Dr. Hirose is a Fellow of the IEICE and a member of JNNS and APNNS.